OPTICS

Simultaneous head-mounted imaging of neural and hemodynamic activities at high spatiotemporal resolution in freely behaving mice

Ningbo Chen[1,2]†, Zhiqiang Xu[1]*†, Zheng Song[1]†, Jiuling Liao[1]†, Hongdong Zhang[1,3], Jiahao Li[1,4], Taofeng Wu[1], Weilei Ma[1], Tiancheng Lei[1], Liangjian Liu[1], Guangying Ma[1], Hui Liao[1], Shiwei Ye[1], Jing Meng[3], Liang Song[1], Puxiang Lai[4], Yingjie Zhu[5], Kenneth K. Y. Wong[2], Hairong Zheng[6]*, Wei Zheng[1]*, Chengbo Liu[1]*

Exploring the relationship between neural activity and cerebral hemoglobin-oxygenation responses in freely behaving mice can advance our understanding of neurovascular coupling. Head-mounted microscopes enable neuroimaging in freely behaving mice; however, investigating neurovascular dynamics remains challenging because of a lack of hemodynamic information, especially blood oxygenation, or insufficient resolution. Here, we report a head-mounted microscope for neurovascular imaging that enables the simultaneous recording of neuronal burst firing and multiparametric hemodynamics such as vascular oxygen saturation at high spatiotemporal resolution. The 1.7-gram lightweight microscope integrates confocal fluorescence and photoacoustic microscopy, allowing recordings at 0.78 hertz with 1.5-micrometer lateral resolution across a field of view of 400 micrometers by 400 micrometers. We identified cell type–specific neurovascular responses to hypoxic challenges, observed active regulation of arterioles during sensory stimuli, and detected abnormal oxygen depletion and vasodilation preceding burst neuronal discharges in epileptic disorders. This technique provides valuable insights into neurovascular coupling and holds potential for studying the pathology of neurological brain diseases.

INTRODUCTION

Neural activity is closely related to blood flow and oxygenation in the brain; this is known as neurovascular coupling (NVC) (*1*, *2*). When a localized area of the brain generates neural activity, the metabolic demand in that region increases, leading to an increase in blood flow to supply more oxygen and glucose to meet the metabolic needs of neurons (*3*). Conversely, if cerebral vessels are unable to supply sufficient oxygen and energy due to pathological changes, then the functional activity of the corresponding brain region will be substantially affected (*4*). Conventional NVC imaging techniques, such as functional magnetic resonance imaging, indirectly infer the brain neural activity based on hemodynamic changes; this sometimes leads to ambiguities in the data interpretation (*5*). Developing imaging methods that directly and simultaneously map the neural activity and hemodynamics will aid in the more accurate interpretation of the neuronal and vascular coupling relationships and the refinement of the biophysical models based on the functional magnetic resonance imaging signals. Moreover, concurrently capturing neural activity and brain

functional information such as blood-oxygen metabolism (*6*) could provide insights into neurological disorders (*7*, *8*) such as epilepsy, Alzheimer's disease, stroke, and migraines. Furthermore, correlating the neural activity and hemodynamic response helps to accurately decode the functional brain activation and facilitate the development of the next-generation brain-computer interface technologies (*9*).

Advanced optical imaging techniques, exemplified by fluorescence imaging modality, have provided powerful means to reveal the mechanism underlying NVC by visualizing spatiotemporal neurovascular dynamics in the rodent brain (*10*, *11*). Most of these studies have been carried out in anesthetized or head-fixed mice with a desktop optical microscope to minimize motion artifacts during imaging. However, anesthesia is known to have profound effects on neuronal activities (*12*). Head-fixed imaging will restrict the natural behavior of mice and substantially limit the exploration of NVC, as the brain's actual response often depends on the animal's behavioral state and environmental interactions. To meet this challenge, several head-mounted microscopes (*13*–*17*), including laser-scanning multiphoton microscopy (two-photon or three-photon) and camera-based single-photon microscopy, have been reported to explore brain activity in freely moving mice. In laser-scanning multiphoton head-mounted systems, two separate optical fibers (*13*, *14*) or a double-clad fiber (*15*) is used in the probe to transmit the illumination laser beam and collect emitted fluorescence photons; these systems provide high resolution and strong contrast with a relatively deep imaging depth. However, head-mounted blood-oxygen imaging has not yet been achieved with such systems. Camera-based single-photon head-mounted systems typically use light-emitting diodes of various colors as illumination light sources and a complementary metal-oxide semiconductor sensor to detect the emitted fluorescence or reflected light within a miniature probe (*16*). These setups provide a large field of view (FOV), fast imaging frame rate, and the ability to

[1]Research Center for Biomedical Optics and Molecular Imaging, Key Laboratory of Biomedical Imaging Science and System, Shenzhen Institute of Advanced Technology, Chinese Academy of Sciences, Shenzhen 518055, China. [2]Department of Electrical and Electronic Engineering, The University of Hong Kong, Pokfulam Road, Hong Kong, China. [3]School of Computer, Qufu Normal University, Rizhao 276826, China. [4]Department of Biomedical Engineering, The Hong Kong Polytechnic University, Kowloon, Hong Kong, China. [5]Shenzhen Key Laboratory of Drug Addiction, The Brain Cognition and Brain Disease Institute, Shenzhen Institute of Advanced Technology, Chinese Academy of Sciences, Shenzhen 518055, China. [6]Lauterbur Research Center for Biomedical Imaging, Key Laboratory of Biomedical Imaging Science and System, Shenzhen Institute of Advanced Technology, Chinese Academy of Sciences, Shenzhen 518055, China.
*Corresponding author. Email: zq.xu@siat.ac.cn (Z.X.); hr.zheng@siat.ac.cn (H.Z.); zhengwei@siat.ac.cn (W.Z.); cb.liu@siat.ac.cn (C.L.)
†These authors contributed equally to this work.

integrate multiple wide-field optical imaging modes to capture both neural activity and cerebrovascular changes (*17*). However, these systems are generally restricted to superficial layers and have limited resolution and contrast, which are severely compromised by tissue scattering and out-of-focus background signals. Therefore, the reported head-mounted microscopes present challenges in investigating neurovascular dynamics because of a lack of hemodynamic information, especially blood oxygenation, or insufficient resolution.

Integrating fluorescence microscopy and photoacoustic microscopy (PAM) (*18–21*) into a head-mounted system is a highly promising approach to achieving simultaneous recording of neuronal activity and hemodynamic with high resolution in freely behaving mice. Fluorescence microscopy allows long-term observation of neurons labeled with specific markers, while PAM leverages hemoglobin absorption for label-free imaging of cerebral hemodynamics. Although numerous dual-modal photoacoustic and fluorescence (PA/FL) microscopes have been implemented (*22–31*), several technical challenges impede their application in head-mounted imaging of mice. In these implementations, transmission mode (*22, 23*) is the most common setup, where an objective lens is positioned on one side of the sample to deliver laser beams and collect fluorescence signals, while an ultrasonic transducer (UT) is placed on the opposite side to detect photoacoustic signals. Although transmission mode enables high-resolution dual-modal imaging, it is only suitable for thin samples. Reflection-mode PA/FL systems can be implemented using an optical-acoustic combiner (*24, 25*). However, this approach increases the imaging probe's size and weight, making it unsuitable for head-mounted imaging in mice. Moreover, the combiner increases the distance between the objective lens and the sample, limiting the use of high–numerical aperture (NA) objectives, which are essential for high-resolution imaging. While a needle UT can reduce the complexity of the probe in a PA/FL system (*26*), it still remains too large for head-mounted applications. Transparent UTs overcome the limitations of traditional piezoelectric transducers by allowing the passage of laser beams (*27*), eliminating the need for bulky combiners, but transparent UTs risk laser damage and introduce aberrations detrimental to high-resolution fluorescence imaging. Optical sensors for photoacoustic detection offer new opportunities for implementing PA/FL systems (*28–30, 32*). For example, optical fiber sensors based on the microring resonator not only exhibit high detection sensitivity and bandwidth but also can be seamlessly integrated into fluorescence microscopes due to their optical transparency and miniaturized size (*30, 32*). However, optical sensors necessitate an additional optical fiber to deliver the detection laser beam to the head-mounted probe that complicates the manufacturing and assembly of the probe (*33*). Moreover, many types of optical sensors are susceptible to vibrations and prone to damage or contamination, and their stability is difficult to maintain in the complex scenarios of freely moving imaging. The PA/FL endoscope, as reported in (*31*), features a compact and tiny imaging probe that uses a multimode fiber to deliver excitation laser beams and collect fluorescence signals, along with another optical fiber to detect acoustic signals based on Fabry-Pérot sensing. However, their imaging quality is relatively limited because of suboptimal laser focusing and low fluorescence collection efficiency, making them immature for head-mounted brain imaging.

Here, we report a head-mounted microscope optimized for NVC imaging at high spatiotemporal resolution and contrast with a lightweight miniature design. In the proposed system, confocal fluorescence microscopy (CFM) (*34*) and PAM are integrated. We initially optimize the optomechanical design and acoustic detection scheme of the imaging probe to minimize its size and weight. In the probe, a dual-axis microelectromechanical system (MEMS) scanner is used to attain rapid optical scanning at a frame rate of 0.78 Hz, a miniature objective with a high NA (0.5) is used to achieve a lateral resolution of 1.5 μm, and a pint-sized (0.4 mm by 0.5 mm by 0.25 mm) high-frequency (center frequency, 55 MHz) flat-field UT is applied to realize the high-sensitivity detection of photoacoustic signals in an FOV of 400 μm by 400 μm. The small size of the UT ensures efficient integration of the CFM and PAM systems by eliminating the need for optical-acoustic beam combiners, such as prisms or coverslips, enabling the development of a compact and lightweight imaging probe (1.7 g). Moreover, compared to optical sensors used for head-mounted imaging, the miniature UT offers stability for long-term imaging and simplifies system setup by eliminating the need for an additional detection optical fiber. In our design, only a single optical fiber is used in the probe to transmit three illuminating laser beams for both the CFM and PAM modalities; concurrently, emitted fluorescence photons are collected for confocal fluorescence detection, and the behavioral interference in mice associated with the use of multiple fibers is eliminated. Furthermore, we demonstrate the potential applications of the proposed head-mounted microscope in NVC research through a series of proof-of-concept experiments in freely behaving mice; these experiments include systemic prolonged hypoxia, localized and rapid electrical stimulation, and epilepsy imaging. These diverse experimental paradigms fully validate the NVC imaging capabilities of this microscope. Overall, our technique provides a tool for NVC research and has the potential to reveal the pathomechanisms of multiple brain diseases by providing a more holistic view of the brain NVC function.

RESULTS

Head-mounted dual-modal imaging platform

The aim of the head-mounted dual-modal imaging platform is to achieve synchronous observations of the neuronal activities and hemodynamic responses in freely behaving mice. To this end, we designed a custom platform that integrates two imaging mechanisms, PAM and CFM (Fig. 1A). For the PAM modality, cerebrovascular morphology data can be acquired label-free. Leveraging the photoacoustic spectral unmixing technique, blood oxygen saturation (sO_2) dynamics can be tracked; that is, on the basis of the distinct absorption characteristics of oxyhemoglobin (HbO_2) and deoxyhemoglobin (HbR) in the visible wavelength range (Fig. 1B), the relative proportion of HbO_2 can be inferred, revealing the oxygen metabolism function of the vasculature. To ensure the optimal photoacoustic spectral unmixing performance, we engineered a dual-channel, pulse-to-pulse wavelength-switching laser source on the basis of the stimulated Raman scattering (SRS) effect (see Materials and Methods and fig. S1). Notably, to prevent background noise in the fluorescence signal due to the overlap of photoacoustic excitation wavelengths and the fluorescence emission spectrum, we red shifted the pulsed pumps to 558 and 570 nm using the Raman frequency shift effect. As a result, the transmission bandwidth of the fluorescence emission filter can be extended to 50 nm (central wavelength, 525 nm; ET 525/50 m; Chroma). This bandwidth covers most of the fluorescence emission spectrum of genetically encoded calcium indicator 6s (GCaMP6s), which allows sufficient transmission of the fluorescence
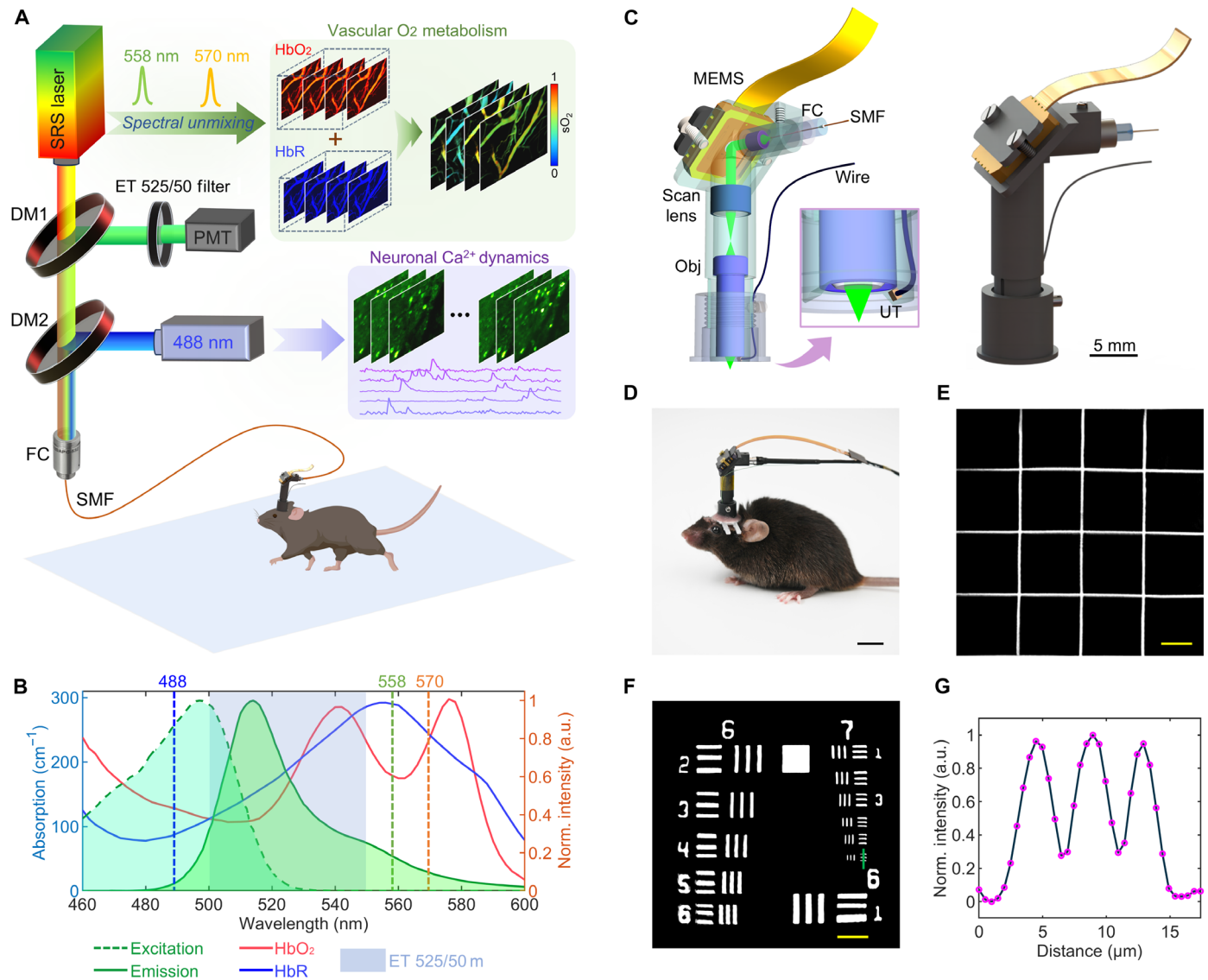
Fig. 1. Head-mounted dual-modal imaging platform. (**A**) Schematic of simultaneous imaging of vascular oxygen metabolism and neural Ca^{2+} dynamics in freely moving mice. FC, fiber collimator. (**B**) Spectral curves. Left axis: Absorption spectra of HbO_2 and HbR. Right axis: Fluorescence excitation and emission spectra of the GCaMP6s calcium indicator. The middle rectangular shading represents the bandwidth of the fluorescence filter (ET 525/50 m). The colored vertical dashed lines indicate the wavelengths (488, 558, and 570 nm) used for dual-modal imaging. a.u., arbitrary units; Norm., normalized. (**C**) Design of the miniature microscope. Left: Transparent three-dimensional (3D) view showing the internal path, light path (green), and mechanical assembly of the head-mounted probe; the inset shows the acoustic detection scheme using a miniaturized UT. Right: The solid model of the probe. Obj, objective. Scale bar, 5 mm. (**D**) Photograph of a freely moving mouse wearing the head-mounted dual-modal microscope. Scale bar, 1 cm. (**E**) FOV measurement by imaging a grid array with 100-μm grid spacing. Scale bar, 50 μm. (**F**) Spatial resolution test using a 1951 USAF resolution test target. Scale bar, 40 μm. (**G**) Cross-sectional intensity profile along the green line in (F); the spacing between the lines in element 6 (group 7) is approximately 2.2 μm.

signal during simultaneous imaging and precisely eliminates interference from the photoacoustic wavelength in fluorescence detection (Fig. 1B). For the CFM modality, we selected a commercial 488-nm continuous-wave laser (OBIS 488LX, Coherent) as the fluorescence excitation source. The excitation beams of both the PAM and CFM modalities were combined via two long-pass dichroic mirrors (DM1, T550lpxr; DM2, ZT488rdc; Chroma). Last, the combined beam was coupled to a single-mode fiber (SMF) and output to the distal head-mounted probe. For the detailed optical path layout, please refer to fig. S1.

In particular, one SMF was used for excitation light transmission and fluorescence collection, and only the in-focus fluorescence was allowed to pass through the fiber-based pinhole (fig. S2) before being detected by a photomultiplier tube (PMT) (CH345, Hamamatsu). The shared pinhole configuration enables cofocusing of the excitation and emission light, which makes the alignment more flexible and the optical path more stable and compact than the conventional method of adjusting individual spatial pinholes to cofocus the emission and excitation light, thus making the miniaturization of the probe feasible. To improve the signal-to-noise ratio of fluorescence

imaging, we further reduced the background noise. For example, angle polishing and antireflection coatings were applied to the fiber end faces to reduce noise from reflected light; low-autofluorescence adhesive (EPO-TEK 301, Epoxy Technology) was used to fabricate fiber-optic connectors; and we carefully selected a carbon polyimide–coated SMF [SM1250SC(9/125)CP, Fibercore] instead of a conventional acrylate-coated SMF to prevent autofluorescence interference.

The head-mounted imaging probe features a lightweight, miniature design (see Fig. 1C and Materials and Methods), with a total mass of only 1.7 g; thus, it is suitable for experiments involving freely moving mice (Fig. 1D). Quantitative comparisons revealed no significant changes in the mice's average movement speed and total travel distance ($n = 4$ mice, two-sided paired t test, $P = 0.3750$ for total distance, $P = 0.2500$ for average speed) while the probe was worn on the head (fig. S7). A custom miniaturized UT was created to accommodate the short working distance of 1 mm underwater imposed by the high-NA (0.5) objective lens. A high NA is a key factor in determining the high fluorescence collection efficiency and superior optical performance of this probe. The FOV of the probe was measured by a grid test target (R1L3S3P, Thorlabs) with 100-μm grid spacing, and an FOV of ~400 μm by 400 μm was achieved (Fig. 1E). To demonstrate the imaging capability, we imaged a 1951 United States Air Force (USAF) resolution test target (R3L3S1P, Thorlabs) (Fig. 1F). The cross-sectional intensity profile along the green line in Fig. 1F was clearly resolved (Fig. 1G), and the spacing between the lines in element 6 (group 7) was approximately 2.2 μm (see Supplementary Text and fig. S2 for the detailed optical design and resolution quantification). Using a miniaturized dual-axis MEMS scanner for laser scanning, we allocated 1.28 s for each 256-pixel by 256-pixel CFM frame, ensuring a sufficient pixel dwell time for optimal fluorescence signal accumulation. For the PAM modality, the images have dimensions of 256 pixels by 250 pixels when the laser frequency is fixed at 50 kHz. To facilitate data processing, we uniformly resized photoacoustic images to match the pixel dimensions of the fluorescence images, i.e., 256 pixels by 256 pixels. In addition, simultaneous exposure to multiple excitation lasers may pose a potential risk of fluorescence photobleaching. To assess this risk, we conducted extended imaging (30 min) to evaluate the effect of photobleaching (fig. S8). By statistically comparing the average fluorescence intensity of neuronal cells during the first and last 5 min, we found no significant evidence of photobleaching ($n = 12$ neurons, two-sided paired t test, $P = 0.7150$). The scanning control, timing synchronization, and acquisition-triggering functions of the imaging platform were implemented on the basis of field-programmable gate arrays (FPGAs) (see Materials and Methods and fig. S3). Thus far, we have completed the hardware design and setup of the head-mounted dual-modal imaging platform. Because of its superior spatiotemporal resolution, real-time recording of the dual-modal information at the cellular scale and investigating the neuronal activities and hemodynamics in freely moving mice are possible; in addition, the complementary dual-modal information provides a novel perspective for further studies of NVC.

Neurovascular response to hypoxia

The brain is highly dependent on oxygen supply, and cerebral hypoxia is a predisposing factor for various neurodegenerative diseases (35). The regulation mechanisms of cerebral neurons and the vascular system under hypoxic conditions remain unclear; therefore, concurrently resolving individual neuron and cerebral vessel responses with high spatiotemporal resolution contributes to improving our understanding of the pathogenesis of hypoxia-induced neurological disorders. In this experiment, we directly altered the inspired oxygen concentration in mice by mixing nitrogen (N_2) in air and continuously monitored the neuronal and cerebral hemodynamic responses of freely moving mice via the proposed head-mounted microscope, and an overhead camera was used for real-time recording of the mouse behavior (see Fig. 2A and Materials and Methods). This experiment could be used to validate the neurovascular imaging performance of our dual-modal imaging platform under systemic stimulation, and it could also provide insights into the regulatory mechanism of NVC for oxygen delivery in the brain.

In the experiment, we observed significant changes in neuronal calcium signaling, hemodynamics, and activity behavior in mice under hypoxia conditions compared to normoxia and recovery period after hypoxia conditions (Fig. 2B and movie S1). Specifically, we extracted all neuronal cells within the FOV, and by averaging all extracted neuronal traces, we found a complicated trend in the neuronal responses under hypoxia conditions; here, the highest peak positive response reached $97.05 \pm 24.29\%$ $\Delta F/F$, and the peak negative response reached $49.19 \pm 9.46\%$ $\Delta F/F$ [Fig. 2C (a), $n = 106$ neurons in one mouse]. Next, fractional changes in total hemoglobin (HbT), HbO_2, and HbR were quantified, revealing that although the changes in the HbT concentration were not large (within 12%) during hypoxia, the relative HbR concentration markedly increased by $137.40 \pm 29.24\%$, whereas the HbO_2 concentration decreased by $38.75 \pm 5.97\%$ [Fig. 2C (b)]. Moreover, the sO_2 level decreased substantially by $36.49 \pm 2.74\%$ [Fig. 2C (c)]. In addition, during hypoxia, some of the blood vessel diameters were dilated by as much as $37.53 \pm 4.34\%$ [Fig. 2C (d)]; through this regulatory mechanism, the blood flow and oxygen delivery could be increased to maintain the proper functioning of the brain (36). The dynamic rebound of cerebral sO_2 after vasodilatation [indicated by the arrow in Fig. 2C (c)] was directly observed using our technique. Statistical analysis indicated that the systemic hypoxic stimulus led to a significant decrease in sO_2 level of $35.03 \pm 7.19\%$ (Fig. 2D, $n = 6$ trials from three mice, two-sided paired t test, $P = 0.0052$) and a significant increase in vessel diameter of $20.26 \pm 4.68\%$ (Fig. 2E, $n = 6$ trials from three mice, two-sided paired t test, $P = 0.0078$); afterward, the values recovered to the baseline levels. Unless otherwise mentioned, the mean of the first 50 frames of the normoxic state data was used as the baseline for calculating the change in each parameter in the quantitative analysis; a five-point moving window was used for data smoothing. By further analyzing the correlation between neuronal calcium dynamics and sO_2 changes, we found a particular NVC relationship, with neuronal populations exhibiting completely opposite responses to hypoxia (Fig. 2F). We categorized all the neuronal cells into two groups, i.e., excitatory and inhibitory, on the basis of their correlation with oxygen depletion (Fig. 2, G to I). The distribution of pairwise Pearson correlation coefficients for all extracted neurons shows the distribution of neuronal populations with different coupling responses (Fig. 2J). The cell type–specific NVC may be associated with variations in the vulnerability of different neuronal cells to the neurotoxic effects induced by hypoxia (37). The pathology of hypoxia-mediated neurologic dysfunction needs to be elucidated further in the future.

Neurovascular response to sensory stimulus

Distinct from the global prolonged hypoxic stimulation described above, we next demonstrated the ability of the proposed dual-modal
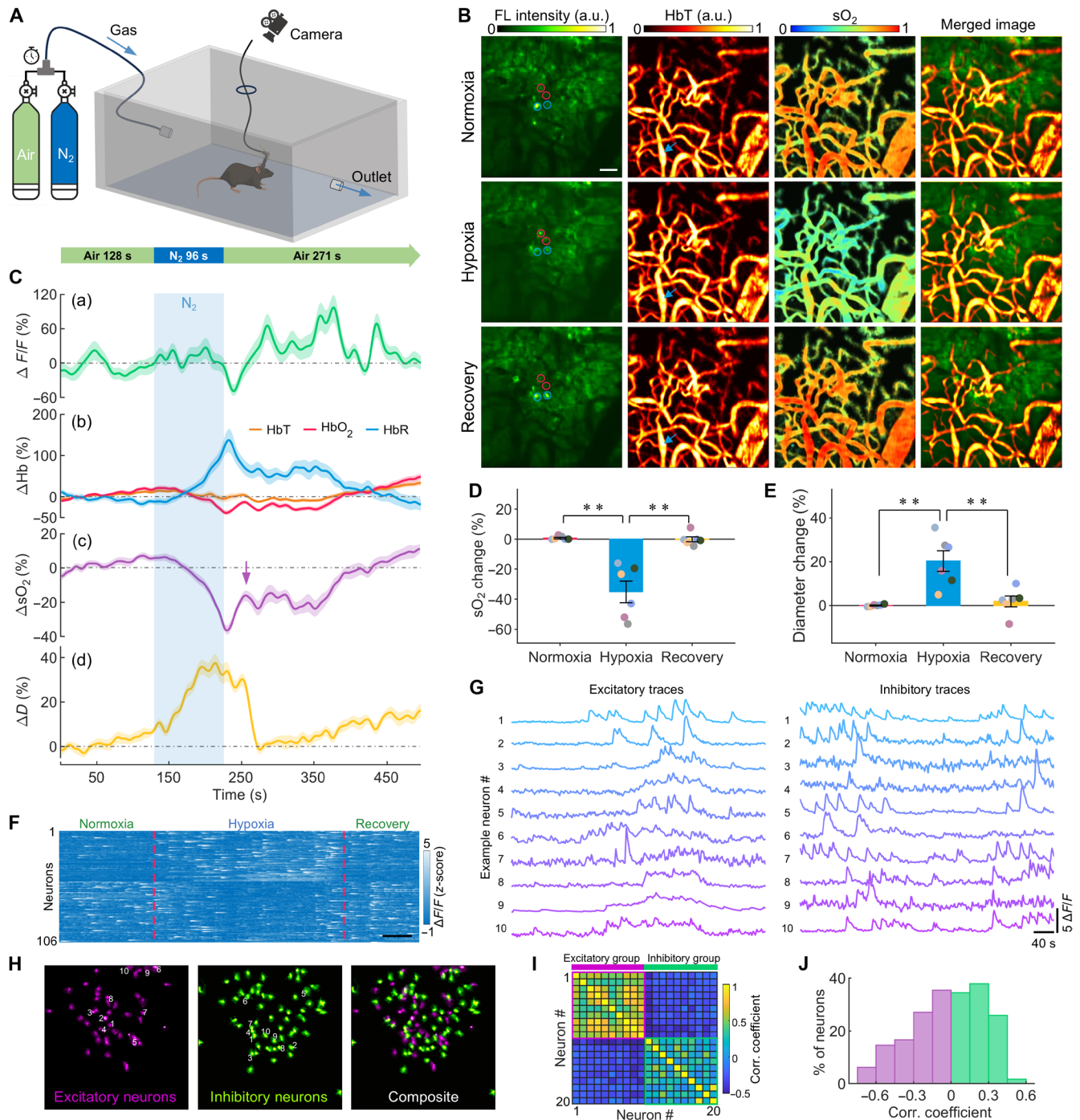
Fig. 2. Neurovascular response to hypoxia. (**A**) Schematic of the hypoxia test paradigm. Pure N_2 and air gases were used to create normoxic and hypoxic environments. (**B**) Synchronized acquisition of dual-modal images during normoxia (top), hypoxia (middle), and recovery (bottom) states. Columns from left to right: Ca^{2+} fluorescence images, photoacoustic images of HbT and sO_2, and merged images. Each image represents a single moment under different states. Red and blue circles mark typical excitatory and inhibitory neurons. Scale bar, 50 μm. (**C**) Neuronal and hemodynamic responses to oxygen changes. (a) Average Ca^{2+} dynamic change from all neuronal traces; (b) overall hemoglobin (Hb) concentration changes within the FOV, with fractional changes in HbT, HbO_2, and HbR concentrations plotted separately; (c) overall blood sO_2 change; (d) vessel diameter change indicated by the blue arrow in (B); results are presented as means ± SEM. (**D**) Statistical comparisons of sO_2 variations in normoxia, hypoxia, and recovery states ($n = 6$ trials over three mice, two-sided paired t test, **$P < 0.01$). The data are presented as means ± SEM. (**E**) Statistical comparisons of vessel diameter changes measured in the normoxia, hypoxia, and recovery states ($n = 6$ trials over three mice, two-sided paired t test, **$P < 0.01$). The data are presented as means ± SEM. (**F**) Heatmap of the calcium transients from all neurons. Scale bar, 40 s. (**G**) Example traces of calcium transients from excitatory (left) and inhibitory (right) neurons, classified by correlation with overall blood oxygen change in the FOV. (**H**) Neuronal population classification based on hypoxia response: excitatory (left), inhibitory (middle), and composite (right). Numbers 1 to 10 indicate neuronal locations in (G). (**I**) Interneuron correlation coefficient matrix for neurons in (G). (**J**) Distribution of pairwise Pearson correlation coefficients of all extracted neurons.

head-mounted microscope to monitor localized NVC responses. This was achieved by observing the neurovascular reactions in specific brain regions under highly localized and rapid stimulus. Electrical foot shock can activate sensory neurons and induce neurochemical changes in the peripheral nervous system. It is a classic paradigm for studying neuropsychiatric disorders in animals (*38*). Here, we simultaneously monitored neuronal and hemodynamic responses in the primary somatosensory cortex (S1) evoked by electrical stimulation on freely moving mice. During the experiment, the mice were allowed to freely move in an electric foot shock apparatus. An externally connected, isolated pulse stimulator provided current pulses for foot stimulation (amplitude, 3 mA; pulse duration, 0.25 ms; frequency, 5 Hz), and an overhead camera was used for real-time recording of the mouse behavior (see Fig. 3A and Materials and Methods). A total of four rounds of electrical stimulation were administered in this experiment, and the dual-modal imaging system accurately captured the changes in neuronal firing, vasomotion, and cerebral oxygenation status in the mice before and during electric shock (Fig. 3B).

To accurately quantify electrical stimulation–induced changes in single neuronal somatic signals, we extracted all cells within the FOV. The example trace of the neuronal calcium transients reflects the activation of somatosensory cortical neurons caused by electrical stimulation, and repeated and consistent results can be observed (Fig. 3, C and D). According to the trajectories of the four rounds of electric shock, the movement speed of the mouse markedly increased after the onset of the electric shock (Fig. 3E and movie S2). The highest peak response of the neuronal signal after the onset of electrical stimulation reached $202.23 \pm 51.08\%$ $\Delta F/F$ (Fig. 3F, $n = 10$ example neurons in one mouse). In addition, we analyzed the hemodynamic parameters of pial arterioles and venules, namely, sO_2, HbT, and vessel diameter (Fig. 3, G to I). The peak sO_2 responses to electrical stimulation were 22.47 ± 8.07 and $6.70 \pm 3.78\%$ greater than the baseline sO_2 in venules and arterioles, respectively. The sO_2 response to neuronal firing was weak in the arterioles, indicating that arterioles still maintain high oxygenation levels despite the increased neural activity caused by sensory stimuli. This suggests that arterioles serve an essential function in preserving a safe margin of tissue oxygenation (*39*). Moreover, the increased sO_2 response in the venules implies that oxygen delivery under a sensory stimulus far exceeds oxygen depletion. Typically, functional hyperemia mechanisms ensure rapid increases in blood flow and oxygen delivery during brain activation, with vessel diameter changes being the most important determinants of blood flow (*40*). By further analyzing the HbT concentration (Fig. 3H) and vessel diameter (Fig. 3I), we found that the responses in the arterioles were strongly related to neuronal firing (Fig. 3F). The largest changes in both HbT concentration and vessel diameter were significantly greater in arterioles than in venules (ΔHbT, $12.82 \pm 6.21\%$ versus $3.94 \pm 5.21\%$; ΔD, $19.03 \pm 3.36\%$ versus $7.14 \pm 1.33\%$). This finding also validates the critical role of the arterioles in regulating cerebral blood flow and oxygen supply (*36*). In contrast, the weaker hemodynamic response of the venules was more likely to be a passive result of changes in upstream blood flow rather than an active regulation mechanism (*41*).

To illustrate the spatial correlation between neuronal activities and hemodynamic responses, we generated adjacency matrices (see Materials and Methods) by calculating Pearson's correlation coefficient between the calcium dynamics of each neuron and the hemodynamics of each blood vessel segment (Fig. 3, J and K). Horizontal analysis of the adjacency matrices revealed that most neurons (labeled 1 to 16)

exhibited correlation with cerebral hemodynamics in this experiment, whereas correlations for some neurons (labeled 17 to 20) were negligible. This may reflect functional heterogeneity among neurons in NVC. Vertical analysis of the adjacency matrices demonstrated that the diameters of arterioles (labeled 1 to 8) showed pronounced correlations with neural activity, while their blood oxygenation exhibited weaker or negligible correlations. In contrast, both the diameters and blood oxygenation of large venules (labeled 9 to 12) displayed moderate correlations with neural activity, whereas correlations for the remaining smaller vessels (labeled 13 to 20) were negligible. These observations highlight the differences in NVC across various vascular types and corroborate the phenomena observed in Fig. 3 (G to I). Specifically, during electrical stimulation, arterioles exhibited the most pronounced diameter changes, while their oxygenation levels remained relatively stable, making oxygenation changes less detectable. Venules, potentially acting as passive conduits for upstream blood flow changes, showed more noticeable diameter and oxygenation changes in larger venules compared to smaller venules and capillaries, likely due to their greater capacity for blood drainage. The results of our high spatiotemporal resolution imaging platform provide a new perspective on sensory-evoked NVC, enabling accurate identification of the functions of both arterioles and venules.

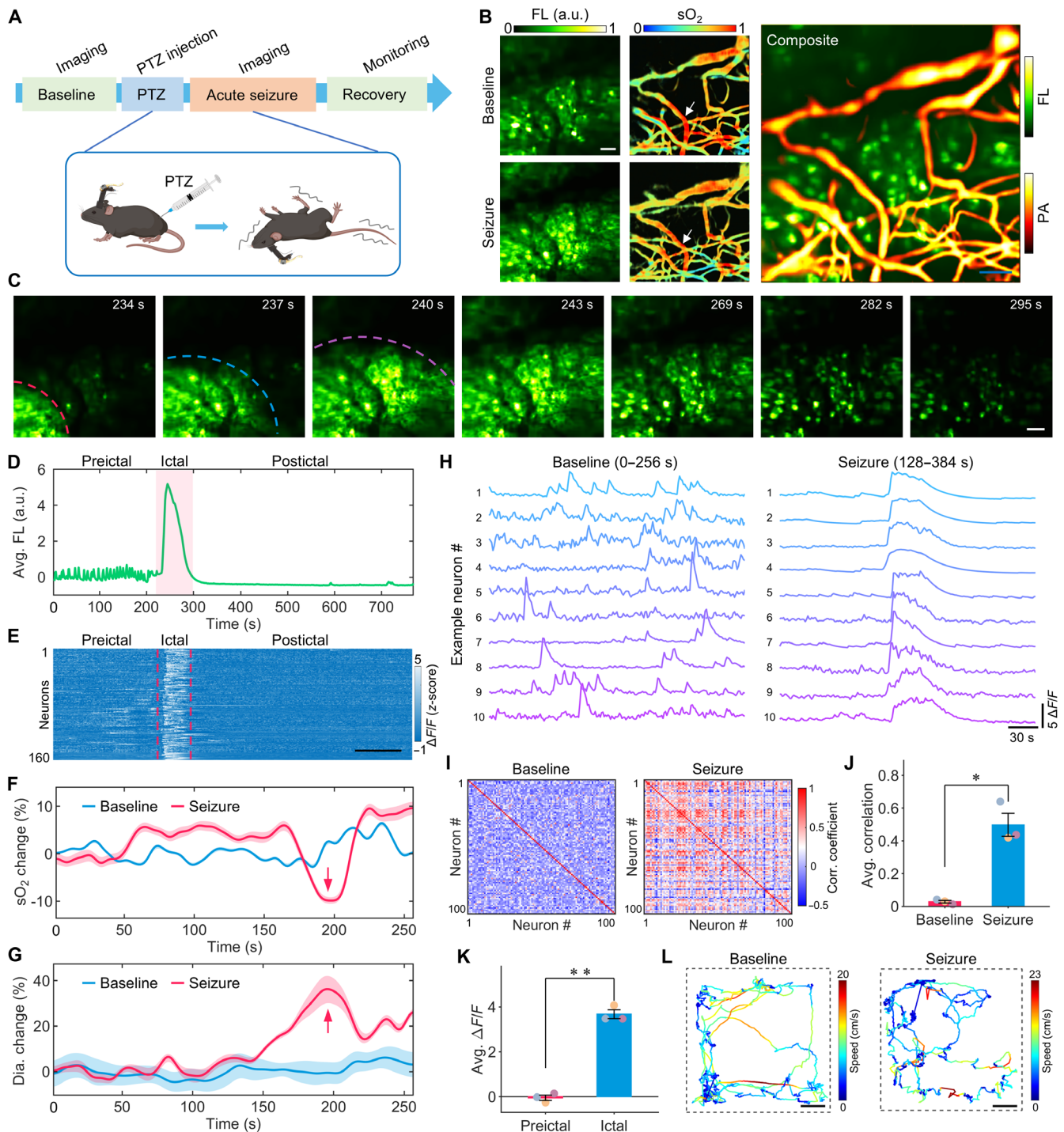## Neurovascular response to acute epileptic seizures

As a final demonstration, our aim was to explore the NVC response in brain pathophysiology. To demonstrate this, we imaged epilepsy-induced NVC in freely moving mice. Epilepsy is known to be one of the most severe brain conditions (*42*), and understanding how this abnormality affects the NVC is essential for revealing potential therapeutic targets for seizures. In the experiment, pentylenetetrazole (PTZ), a well-established agent for inducing acute epilepsy in mice, was used to induce the epilepsy model, and seizure initiation and propagation in freely moving mice were visualized through our miniature head-mounted microscope (see Fig. 4A and Materials and Methods). Representative neurovascular maps during the baseline (pre-PTZ injection) and seizure periods were examined, and the high-resolution image obtained by fusing the imaging results of neuronal soma and cortical vessels demonstrates the in vivo imaging capabilities of the proposed system at the cellular scale (Fig. 4B).

Epileptic seizures are characterized by hypersynchronous discharges, and understanding their precise propagation can provide clues for the prediction and suppression of epilepsy (*43*, *44*). Leveraging the high spatiotemporal resolution of the proposed system, we successfully observed the dynamic progression of seizures, with the wavefront rapidly expanding into neighboring regions (Fig. 4C and movie S3). We analyzed the change in the calcium signal over the overall image, revealing that in the preictal buildup period, neuronal ensembles present high-frequency low-intensity microepileptic seizures, which last for approximately 200 s, followed by bursts of high-intensity discharges when the epileptic buildup reaches a localized threshold (Fig. 4D), which signals the onset of epileptic wave propagation. A heatmap of the calcium transients from all neurons revealed a marked ictal discharge in the seizure state (Fig. 4E). Through comparisons with the baseline state, we found that the hemodynamic responses of the mouse markedly differed in the seizure state. High-frequency neurological activation during the epileptic buildup (i.e., preictal) period led to the depletion of a substantial amount of oxygen, with a $9.88 \pm 0.67\%$ decrease in sO_2, which was accompanied by a transient vasodilatation of $36.20 \pm 6.04\%$ (Fig. 4, F and G). The
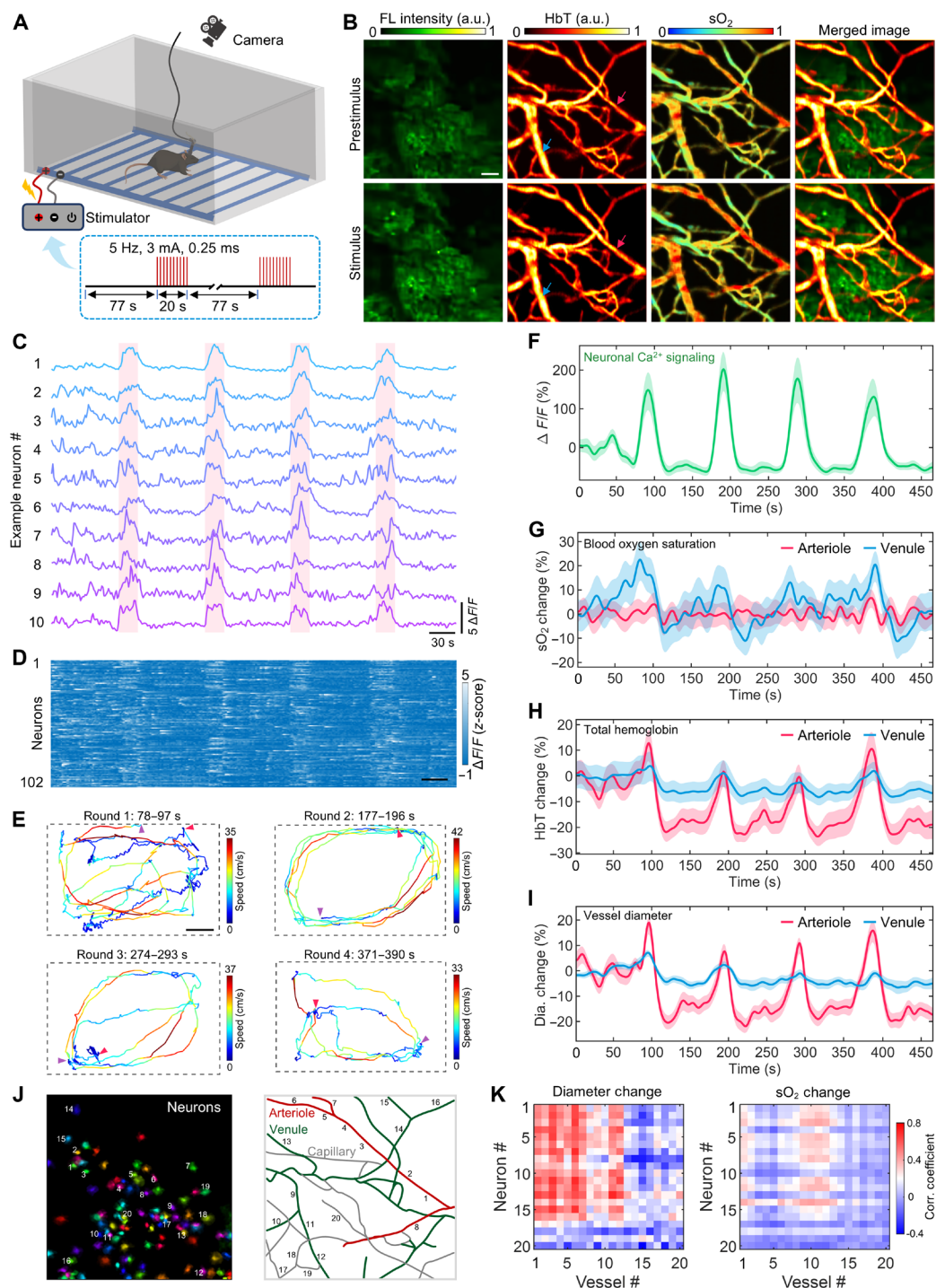
Fig. 3. Neurovascular response to sensory stimulus. (**A**) Schematic showing the foot shock setup and the electrical stimulus signal setting. The monophasic electric pulse trains had a 3-mA pulse amplitude and 0.25-ms pulse duration at a frequency of 5 Hz. (**B**) Synchronized acquisition of dual-modal images before (top) and during (bottom) electrical stimulation. Columns from left to right: Ca^{2+} fluorescence (FL) image, photoacoustic image of HbT concentration, photoacoustic image of sO_2, and dual-modal merged image. Scale bar, 50 μm. (**C**) Example trace of calcium transients from 10 neurons. The vertical red shading indicates the electrical stimulus applied. The scale bar applies to all individual traces. (**D**) Heatmap of calcium transients from all extracted neurons. The color bar indicates the z-score normalized $\Delta F/F$ value. Scale bar, 30 s. (**E**) Mouse movement trajectories during four electrical foot shock rounds; the colors denote the moving speeds. The red and purple arrowheads mark the moments at which the electric shock begins and ends, respectively. Scale bar, 5 cm. (**F**) Average Ca^{2+} dynamic change from 10 example neuronal traces in (C); the line and shading denote means ± SEM. (**G** to **I**) Hemodynamic responses of arterioles and venules [indicated by the red and blue arrows in (B), respectively] to electrical foot shock. The changes in sO_2, HbT, and vessel diameter are shown in the figures. The data are presented as means ± SEM. Dia., diameter. (**J**) Segmentation of neurons and blood vessels. (**K**) Adjacency matrices between neuronal dynamics and hemodynamic responses. The sequence numbers of representative neurons and vascular segments, including arteriole, venule, and capillary, are labeled in (J), respectively.

Fig. 4. Neurovascular response to acute epileptic seizures. (**A**) Schematic showing the timing of imaging and PTZ-induced acute epileptic seizures in mice. (**B**) Left: Images of Ca²⁺ dynamics and sO₂ at baseline (top) and during seizures (bottom). Right: Representative overlay of photoacoustic (PA) and fluorescence (FL) images at baseline. Scale bars, 50 μm. (**C**) Ca²⁺ dynamic images from single frames at the indicated time points during seizure wave propagation. Scale bar, 50 μm. (**D**) Average (Avg.) Ca²⁺ dynamic change from all frames of FL images acquired during seizures. The FL intensity is z-score normalized. (**E**) Heatmap of calcium transients from all neurons. The entire epoch can be divided into three periods: preictal, ictal, and postictal, separated by the red dashed lines. Scale bar, 100 s. (**F**) SO₂ changes in blood vessels [indicated by the white arrow in (B)] at baseline versus the seizure state. (**G**) Changes in blood vessel diameters [indicated by the white arrow in (B)] at baseline versus the seizure state. Two sets of data with the same duration (0 to 256 s) were used for comparison. (**H**) Example traces of calcium transients during baseline (left) and seizure (right). Time for baseline data, 0 to 256 s; time for seizure data, 128 to 384 s. (**I**) Interneuron correlation coefficient matrices of Ca²⁺ dynamics from the baseline (left) and seizure (right) states. (**J**) Statistical comparison of average cross-correlation coefficients in the baseline and seizure states ($n = 3$ mice, two-sided paired t test, *$P < 0.05$). The data are presented as means ± SEM. (**K**) Average Ca²⁺ response magnitude in the preictal and ictal states ($n = 3$ mice, two-sided paired t test, **$P < 0.01$). The data are presented as means ± SEM. (**L**) Mouse movement trajectories in the baseline and seizure states; the colors denote the moving speeds. Scale bars, 5 cm.

epileptic NVC results indicate that the hemodynamic changes associated with oxygen depletion and vasodilation precede the onset of ictal neuronal discharges. This provides a timing window for epileptic interventions, and restoring cortical oxygenation may be effective for epileptic suppression (*45*). Furthermore, the calcium transient traces in the baseline and seizure states revealed distinct firing patterns, with the seizure state showing hypersynchronous characteristics (Fig. 4H). Interneuron correlation analysis indicated that the correlation between neuronal activities was enhanced during the seizure state (Fig. 4I). Statistical analysis revealed that the mean correlation coefficient increased from 0.03 ± 0.01 to 0.42 ± 0.12 following seizures (Fig. 4J, $n = 3$ mice, two-sided paired t test, $P = 0.0186$). The statistics showed that the mean $\Delta F/F$ response magnitude increased from -0.05 ± 0.12 in the preictal period to 3.68 ± 0.20 in the ictal period (Fig. 4K, $n = 3$ mice, two-sided paired t test, $P = 0.0068$). The movement trajectories revealed notable differences in both speed and route between the baseline and seizure states in the mice (Fig. 4L and movie S3). In summary, within this brain disease study paradigm, we successfully visualized the initiation and progression of epilepsy in freely moving mice using the high spatiotemporal resolution dual-modal head-mounted microscope. Concurrently, we recorded the dynamic responses of NVC. This advanced technique is anticipated to serve as a valuable reference for further pathological studies of brain diseases.

DISCUSSION

We have presented a miniaturized dual-modal head-mounted microscope dedicated to neurovascular imaging. The microscope uses CFM to track the neuronal calcium dynamics and PAM to capture the structural and functional information from the cerebral microvasculature. This system achieves simultaneous imaging of neuronal activities and the vascular hemodynamic responses in freely moving mice, with a lateral resolution of 1.5 μm over an FOV of 400 μm by 400 μm and a mass of 1.7 g.

We conducted three types of in vivo NVC imaging experiments to validate the capabilities of our dual-modal head-mounted microscope across diverse physiological states. First, in the systemic prolonged hypoxia experiment, we synchronously observed the responses of individual neurons and cerebral vessels to hypoxia in mice. When respiratory oxygen intake decreased, the global oxygen saturation in brain regions markedly decreased; this triggered cortical vasodilatation to regulate oxygen delivery to elevate oxygen saturation in response to the hypoxic challenge. Moreover, hypoxia-induced neuronal activities exhibited notable differences, with some showing inhibitory states and others displaying hyperexcitability. The cellular-level neuronal somatic identification enabled precise categorization of the different neuronal populations. Next, we used the microscope for localized NVC imaging in specific cortical regions. We observed the activation of the neuronal activities in the mouse somatosensory cortex using highly localized and rapid electrical stimuli, and different hemodynamic responses of cortical arterioles and venules were revealed. The active regulation mechanism of arterioles in preserving the safe oxygenation margin in the somatosensory cortex during brain activation by sensory stimuli was visualized. This showed the technique's capability for NVC imaging from systemic to rapid localized stimulation. Last, in the epilepsy imaging experiment, we visualized the initiation and progression of epilepsy in freely moving mice.

This experiment demonstrated the reliability and applicability of the microscope for NVC imaging of brain diseases. We captured the hypersynchronous neuronal firing and the propagation of seizure waves, as well as the hemodynamic responses of blood oxygen depletion and vasodilation due to high-frequency neurological activation. Moreover, using simultaneous dual-modal imaging capabilities, we identified a time window of oxygen depletion and vasodilatation that precedes burst neuronal discharges. This observation could serve as an early warning signal, enabling timely intervention to suppress epilepsy. Together, these proof-of-concept imaging paradigms thoroughly demonstrated the powerful capabilities of the microscope for NVC studies. We anticipate that this technique will be applicable to a wider range of pathological and therapeutic studies on brain diseases in the future.

While we meticulously optimized the key components and optical designs of the microscope and demonstrated its NVC imaging capabilities, some future improvements may further enhance its performance. For example, the FOV is currently constrained by the effective acoustic detection area of the miniaturized UT. The transducer size can be further optimized to accommodate a larger FOV, but it is essential to consider the electrical impedance and the detection sensitivity to achieve optimal performance (see Supplementary Text and fig. S9); the FOV could also be expanded to a millimeter scale by combining multiple UTs in a single imaging probe in future work. In addition, scalable transducer arrays (*46*) are expected to provide a potential solution for extending the FOV. The current system uses a high-NA miniaturized objective to achieve high spatial resolution, which is adequate for identifying individual neurons and microvasculature; however, this compromises the microscope's depth of field (DOF). Future versions could integrate a *z*-scanning module (*47*, *48*) to extend the imaging DOF, although this may necessitate a larger probe size and compromise the lightweight nature of the microscope. Alternatively, developing compact and lightweight diffractive optical elements (*49*, *50*) with multifocal or long depth of focus may be a viable alternative for achieving volumetric imaging with an extended DOF. Moreover, switching from a sawtooth wave to a higher-frequency sinusoidal wave for driving the MEMS scanner could increase the scanning rates and the temporal resolution. However, this approach may introduce field distortion (*51*). An optimized double-spiral resonant scanning scheme (*52*) could alleviate this issue and increase the scanning rate without sacrificing the FOV. In addition, downsampling combined with image restoration algorithms (*53*, *54*) can also help to further accelerate the imaging speed. The degradation of the signal-to-noise ratio due to the shorter integration time for fluorescence detection could be mitigated by developing neural network–based denoising and deblurring algorithms (*55*, *56*). For long-term imaging, especially at high imaging speeds, photobleaching due to overexposure requires careful consideration. Exploring photoacoustic imaging with low laser doses (*57*, *58*) may effectively mitigate this issue. In addition, integrating two-photon or three-photon imaging modalities, which use longer wavelengths and enable more localized fluorescence excitation, will further minimize the risk of photobleaching in out-of-focus regions. This approach also allows for deeper imaging with reduced photodamage to the surrounding areas. With the current outstanding performance of this dual-modal head-mounted microscope and the potential for flexible upgrades and expansions, we believe this technology can provide a better understanding of NVC in neuroscience.

MATERIALS AND METHODS

Design, manufacturing, and assembly of the miniature microscope

The overall design of the dual-modal miniature microscope can be divided into three parts: optical, mechanical, and acoustic detection schemes. For the optical design, we used the optical design software Zemax OpticStudio (2024 R1.00, Ansys) to simulate and optimize the optical path configurations within the miniature probe (fig. S2). Specifically, a custom miniature fiber collimator with a diameter of 3 mm was used to collimate the multiwavelength lasers. This collimator consisted of a glass ferrule to secure the optical fiber, an achromatic doublet lens (#84-125, Edmund Optics), and a metal housing. The collimated laser beams were then reflected by a MEMS scanner (F1M16.2-1600AL, Mirrorcle Technologies Inc.), and the MEMS scanner was actuated by an analog input driver (BDQ PicoAmp 5.4 T180, Mirrorcle), enabling two-dimensional (2D) optical scanning. Last, these beams were relayed by a scan lens (D0226-3×.101, Domilight) and focused onto the biological tissue by an objective lens (D0226-3×/0.5, Domilight).

In the mechanical design phase, computer-aided design software (SolidWorks 2020, Dassault Systèmes) was used to create a 3D solid model of the probe on the basis of the optical simulation results, ensuring precise manufacturing and assembly through geometric dimensioning and tolerancing. Five-axis computer numerical control (CNC) machining was used for manufacturing, and a 30% carbon fiber–reinforced polyetheretherketone material was selected for the housing due to its lightweight properties and robust mechanical strength. The mass of the probe containing all the optical components is 1.7 g; the sleeve and baseplate bonded to the mouse skull have a mass of 0.55 g for a total mass of 2.25 g. The probe's components were designed to be detachable for flexibility, with the MEMS scanner attached to the probe body via M1.2 slotted pan head screws and the scan lens, objective lens, and miniature fiber collimator secured with stainless steel M1.2 slotted flat point set screws. Notably, the use of a customized fine-pitch thread (M5.5, 0.5-mm pitch) on the outer periphery of the probe output end and an internally threaded sleeve fixed on the mouse skull allows for easy disassembly and assembly. This feature provides flexibility for long-term recurring imaging scenarios. In addition, the fine-pitch thread enables precise manual adjustment of the optical focus depth (0.5 mm per revolution). Once the focus depth is confirmed, an M2 hex socket flat point set screw on the sleeve side is firmly tightened, preventing FOV drift caused by the free movement of the mice during imaging (see fig. S4 for the detailed probe assembly procedure).

For the acoustic detection scheme, our probe used a planar unfocused transducer as the acoustic receiving unit. We simulated the acoustic fields of transducers with various physical dimensions using the MATLAB toolbox k-Wave (see Supplementary Text and fig. S9). A 2D size of 0.4 mm by 0.5 mm was selected as the optimal balance between acoustic FOV and detection sensitivity; the excellent acoustic response characteristics of the miniaturized UT (55 MHz central frequency and −6-dB bandwidth of 70%) ensure the accurate recovery of the photoacoustic signal. With the off-axis alignment configuration, the UT can receive ultrasound signals without obstructing the excitation laser and emitted fluorescent signals. Furthermore, we corrected the imaging depth deviations caused by off-axis ultrasonic detection (fig. S5). These deviations arise from the varying times of the ultrasound waves reaching the UT at different positions within the FOV. The UT was securely bonded to the inclined surface at the probe housing end via ultraviolet-curing optical adhesive (NOA61, Thorlabs). The specially designed inclined angle ensures overlap of the acoustic detection path with the optical scanning area, maximizing the detection sensitivity and uniformity within the imaging FOV. In addition, a wiring groove was fabricated on the probe housing to facilitate the passage of the UT's microcoaxial cable [American Wire Gauge (AWG) 46; outer diameter, 0.2 mm; Hitachi Cable].

System control and image acquisition

Synchronization and real-time display of CFM and PAM in the imaging platform were realized by a dedicated data acquisition method (fig. S3). An FPGA card (Zynq 7010, Xilinx) was used to control all the devices at nanosecond timescale, and a global synchronization mechanism was established using custom-built software based on the FPGA. The amplified photoacoustic signal was sampled by an analog data acquisition card (DAQ1; ATS9350, AlazarTech). The fluorescence signal detected by a digital PMT was sampled by another DAQ (DAQ2; PCIe-6323, National Instruments). Both the DAQ cards were inserted in a workstation (T7920, Dell) via peripheral component interconnect express (PCIe) slots to guarantee sufficient readout speed and frame transmission bandwidth for data saving and display.

During imaging, DAQ2 generated x-axis and y-axis sawtooth drive signals for the MEMS scanner, achieving raster scanning within the FOV. Two pulsed 532-nm lasers were triggered by the FPGA at a frequency of 50 kHz with a fixed time interval, and then dual-wavelength laser beams (558/570 nm) were generated by an SRS module. Photoacoustic signals excited by the two laser beams were recorded by DAQ1 sequentially. At the beginning of each line scan, the rising edge of the x-axis drive signal was synchronized with the trigger signals of 532-nm lasers by the FPGA. DAQ2 recorded fluorescence signals using a digital counter that was synchronized with the trigger signals of 532-nm lasers to ensure the synchronization between CFM and PAM. The FPGA also triggered cameras (MER2-502-79U3M, Daheng Imaging) to obtain synchronized video recordings of the freely moving mice. A memory buffer list was carefully designed within the workstation to enable real-time data processing and display for both PAM and CFM.

Dual-channel output SRS laser source

We engineered a dual-channel, pulse-to-pulse wavelength-switching laser source on the basis of the SRS effect (59) (fig. S1). Two pulsed fiber lasers (VPFL-G-HE-30, Spectra-Physics), both initialized at a 532-nm wavelength with a 3-ns pulse width, were designated pump sources for dual-channel SRS. For the 558-nm SRS channel, we selected a 6.7-m-long single-mode pure silica core polarization maintaining (PM) fiber (HB450-SC, Fibercore) as the Raman gain medium. The incident pulse energy on the PM fiber was finely tuned using a half–wave plate (HWP1; GCL-060712, Daheng Optics) in conjunction with a polarizing beam splitter cube (PBS121, Thorlabs). A second HWP (HWP2; GCL-060712, Daheng Optics) was used to optimize the polarization state, thereby increasing the SRS efficiency and energy output. The input and output ports of the PM fiber were secured with a bare fiber terminator (BFT1, Thorlabs) and a fiber connector coupled with fiber collimators (F220FC-532, Thorlabs) to manage the coupling of the pump light and the collimation of the Raman-shifted light. A 10-nm bandwidth band-pass filter (F1; FBH560-10, Thorlabs) was deployed at the output end to isolate the secondary Stokes wave generated by SRS, specifically the 558-nm laser. The 570-nm SRS output channel had the same optical configuration

as the 558-nm channel, but a slightly longer 10-m PM fiber was incorporated to lower the Raman threshold and facilitate energy transfer to the third-order Stokes wave (570 nm). A 10-nm bandwidth band-pass filter (F2; FBH570-10, Thorlabs) was used to selectively filter out the third-order Stokes wave, yielding a 570-nm wavelength laser.

The dual-channel SRS beams were combined through a long-pass DM (DM3; T565lpxr, Chroma) with a central wavelength of 565 nm. After passing through the DM, the single-pulse laser energy of each channel exceeded 400 nJ, which is far enough to satisfy the energy requirement for in vivo imaging. To ensure the stability of the laser output, we maintained a constant ambient temperature and humidity and minimized disturbances from external air flow and mechanical vibrations. For imaging experiments, adjustable attenuators were used to reduce the energy irradiated to the surface of the living sample to meet the American National Standards Institute (ANSI) safety limits. The single-pulse laser energy at the imaging interface was 60 nJ. The dual-channel pump sources were synchronized via two external trigger signals operating at a 50-kHz pulse repetition rate, incorporating a 2.2-μs time delay between the signals to achieve pulse-to-pulse wavelength switching. Accurate laser power calibration is crucial for reliable sO_2 measurements. Before and after the imaging sessions, we calibrated the laser at the light output end of the probe using a power meter to ensure the consistency of the dual-wavelength laser power. This process guarantees the accuracy of the blood oxygenation monitoring.

Animals
For all in vivo experiments conducted in this study, we used male C57BL/6J mice (6 to 8 weeks old and weighing 20 to 25 g) purchased from Beijing Vital River Laboratory Animal Technology Co. Ltd. These mice were kept in clean cages with ad libitum access to food and water. The ambient temperature was maintained within a range of 18° to 22°C, and the relative humidity was maintained at 50 to 60% to ensure optimal living conditions that minimize stress and promote the health of the animals. All animal experiments were conducted following protocols approved by the Guangdong Provincial Animal Care and Use Committee. In addition, the procedures adhered to the guidelines set forth by the Animal Experimentation Ethics Committee of the Shenzhen Institute of Advanced Technology, Chinese Academy of Sciences.

Surgical procedures
During the surgical procedures, the C57BL/6J mice were anesthetized with a mixture of isoflurane and oxygen (3% for induction and 1 to 1.5% for maintenance) and then fixed on a stereotaxic instrument (68513, RWD Life Science). A temperature controller (69027, RWD Life Science) was used to maintain the mouse's body temperature at 37°C. The hair on the mouse near certain brain regions was carefully removed with scissors and depilatory cream, the scalp was excised, and the periosteum and connective tissue on the surface of the skull were removed using a sharp surgical blade to expose the complete skull. The S1 cortex of each mouse was located via the stereotaxic instrument, and then a high-speed cranial drill (0.5-mm tip diameter) was used to outline a craniotomy with a diameter of 3.5 mm centered on the S1 hindlimb cortex (S1HL; 0.8 mm posterior to bregma and 1.5 mm lateral). The drill bit was repeatedly polished along the circular contour until the skull became thinner at the circle. Throughout the drilling process, the skull was periodically flushed with sterile saline, preventing thermal damage to the cerebral cortex. Once the circular skull fragment was completely

loosened, it was carefully clamped with fine surgical forceps and peeled off.

After the residual debris was removed and any bleeding was stopped, virus injection was performed. The recombinant adeno-associated GCaMP6s virus with the human synapsin promoter ($>2 \times 10^{12}$ vector genomes/ml), purchased from Brain Case (Shenzhen) Biotechnology Co. Ltd., was injected approximately 0.25 mm below the dura mater in S1HL. A total volume of 250 nl was injected via a high-precision nanoliter microinjection pump (Nanoject III, Drummond Scientific) with a fine glass electrode at a speed of 50 nl/min. The electrode remained in the cerebral cortex for 10 min postinjection before being withdrawn slowly. A few drops of 0.6% agarose were subsequently dripped onto the exposed cerebral cortex to fill in the cranial defects. A 50-μm–thick transparent polyvinyl chloride sheet was cut into 4.5-mm–diameter discs and affixed over the craniotomy site. The edges were sealed with tissue adhesive (Vetbond, 3M) to form a stable and transparent window. A mixture of super glue (T-1, Beijing Chemical Works) and denture base powder (Type II, Shanghai New Century Dental Materials) was used to further seal the edges of the cranial window and fill the exposed skull bone. Before the glue mixture solidified, a CNC-machined metal baseplate with a round hole was bonded onto the craniotomy, providing a platform for headpiece attachment in the subsequent procedures. Last, silicone sealant (KWIK-CAST, World Precision Instruments) was applied over the polyvinyl chloride window to protect it from contamination. After surgery, the mice were individually housed in cages and administered antibiotics for seven consecutive days to prevent inflammation and infection, which could compromise the clarity of the cranial window.

Head-mounted microscope installation
During probe installation, first, the miniature probe, fitted with a sleeve, was attached to an adjustable kinematic mount (KM100C, Thorlabs) and connected to a three-axis precision translation stage (GCM-901602M, Daheng Optics) for precise XYZ adjustments. Next, we secured the anesthetized mouse to a custom brain fixation device equipped with a gas anesthesia mask and a heating pad to maintain anesthesia and body temperature, respectively. The mouse's head was firmly affixed to prevent FOV drift upon awakening. We then removed the silicone sealant to expose the cranial window, followed by thorough cleaning with an alcohol-dipped cotton swab. When the mouse awakened, we aligned the probe tip with the baseplate window and used the real-time display in the imaging software to identify the region of interest (ROI). Once the ROI was located, the sleeve was secured to the baseplate. Dental cement, a mixture of dental powder and super glue, was applied to seal and stabilize the imaging ROI. To facilitate the mice's adaptation to the head-mounted probe, a custom replica with the same mass and size as the probe was used for preimaging weight-bearing exercises, ensuring a smoother transition to the actual imaging experiments. After the experiments, a custom slotted flat point screw was attached to protect the cranial window, allowing for quick and consistent identification of the ROI in the long-term and repeated imaging scenarios. The Supplementary Text and fig. S6 show a step-by-step illustration of the head-mounted microscope installation procedure.

In vivo NVC imaging procedures
In vivo hypoxia imaging experiment
For the hypoxia experiments, the mice were kept in a closed hypoxic chamber (30 cm by 20 cm by 20 cm) made of transparent acrylic. Air

nozzles were installed on both sides of the chamber, designated the inlet and outlet for gas-flow regulation. The inlet nozzles were connected to regular air and high-purity nitrogen (purity, ≥99.99%) channels, which could be switched to control the oxygen content in the chamber. The outlet was connected to a vacuum pump for suction and exhaust to facilitate the gas exchange process within the chamber. At the beginning of the experiment, the inlet air pump (R510-29, RWD Life Science) was activated to deliver normal air at a flow rate of 20 liter/min, while the outlet was opened to maintain proper air circulation. Baseline images were captured under normoxic conditions for a duration of 128 s. Then, the regular air supply was shut off, and the nitrogen supply was initiated at a comparable flow rate of 20 liter/min for 96 s. This influx of nitrogen was designed to displace the oxygen in the chamber and establish an artificial hypoxic environment within the chamber. During the nitrogen input process, the mice gradually entered a state of hypoxia and suffocation. The nitrogen supply was subsequently halted, the regular air supply was resumed, and image acquisition was terminated after the mice were observed to return to their normal freely moving state.

In vivo electrical stimulation imaging experiment

In this paradigm, electrical foot shock (*38*) was used as a stressor to provoke a state of fear in mice. The electric foot shock apparatus (31 cm by 21 cm by 20 cm) consisted of transparent acrylic plates and a metal grid floor. The bottom metal grid floor was used to conduct the foot shock current, and the electrical stimulus signal was generated by an isolated pulse stimulator (2100, A-M Systems) connected to the metal grill. Monophasic electric pulse trains were delivered with a pulse amplitude of 3 mA and a pulse duration of 0.25 ms at a frequency of 5 Hz. During the experiment, each electric shock session was 20 s long, and four electric shock cycles were carried out at an interval of 77 s.

In vivo epileptic imaging experiment

An appropriate amount of PTZ (P6500, Sigma-Aldrich) was diluted with 0.9% sterile saline to make a PTZ solution (5 mg/ml) before the experiment. The injection volume of PTZ solution was determined according to the body mass of the mouse to provide a dose of 50 mg/kg (*60*); this value was approximately 200 μl for a mouse with a mass of 20 g. For the imaging session, head-mounted mice were first placed in a transparent acrylic box (30 cm by 30 cm by 20 cm) for habituation, and the baseline images were captured for 4 min before PTZ injection. Then, the imaging was paused, the mouse was removed, and the prepared PTZ solution was slowly injected into the lower right quadrant of the abdomen of the mouse via a 1-ml syringe. Postinjection, the mice were returned to the box, and imaging was resumed to monitor and record the progression of PTZ-induced epileptic seizures. After the experiment, the mice were closely observed until they had recovered from the seizures and were then returned to their home cages.

Statistical analysis

All data are presented as mean with SEM. Two-sided paired *t* tests were used to compare statistical differences between the two groups under different states, and $P < 0.05$ was considered statistically significant. We used Pearson's correlation coefficient as a metric to assess the similarity between the neuronal activities and the changes in oxygen metabolism, as well as the similarity of interneuronal activities across different states. All statistical analyses and their graphing were performed using MATLAB (R2023b, MathWorks). Custom MATLAB scripts were developed for dual-modal image

reconstruction. Raw fluorescence images were first applied with the motion-correction algorithm NoRMCorre (*61*) to reduce the motion artifacts within the FOV. Pseudo-color coding and image fusion were executed using ImageJ (National Institutes of Health). The open-source constrained nonnegative matrix factorization for microendoscopic data (CNMF-E)(*62*) algorithm was used to identify the neuronal cells and extract their calcium signal dynamics ($\Delta F/F$), and all $\Delta F/F$ values were normalized using the *z*-score. For neurovascular spatial correlation analysis, we segmented vascular images and assigned an identifier to each vessel segment. The longer blood vessels were further divided into shorter sections to enhance analytical precision. Then, we calculated the averaged diameter and blood oxygenation level for each vessel segment in every frame. Subsequently, we obtained the dynamics of each blood vessel, including changes in blood diameter and blood oxygenation during the imaging experiment. To illustrate the spatial correlation between neuronal activities and hemodynamic responses, we generated adjacency matrices by calculating Pearson's correlation coefficient between the calcium dynamics of each neuron and the hemodynamics of each blood vessel segment. For behavioral analysis, we used the open source computer vision library (OpenCV)-based channel and spatial reliability tracking (CSRT) (*63*) algorithm to monitor the mouse movement trajectories in the recorded videos.

Supplementary Materials

The PDF file includes:
Supplementary Text
Figs. S1 to S9
Legends for movies S1 to S3
References

Other Supplementary Material for this manuscript includes the following:
Movies S1 to S3

REFERENCES AND NOTES

1. C. Iadecola, The neurovascular unit coming of age: A journey through neurovascular coupling in health and disease. *Neuron* **96**, 17–42 (2017).
2. B. W. Chow, V. Nuñez, L. Kaplan, A. J. Granger, K. Bistrong, H. L. Zucker, P. Kumar, B. L. Sabatini, C. Gu, Caveolae in CNS arterioles mediate neurovascular coupling. *Nature* **579**, 106–110 (2020).
3. J. R. Mester, M. W. Rozak, A. Dorr, M. Goubran, J. G. Sled, B. Stefanovic, Network response of brain microvasculature to neuronal stimulation. *Neuroimage* **287**, 120512 (2024).
4. F. R. Beinlich, A. Asiminas, V. Untiet, Z. Bojarowska, V. Plá, B. Sigurdsson, V. Timmel, L. Gehrig, M. H. Graber, H. Hirase, Oxygen imaging of hypoxic pockets in the mouse cerebral cortex. *Science* **383**, 1471–1478 (2024).
5. E. M. C. Hillman, Coupling mechanism and significance of the BOLD signal: A status report. *Annu. Rev. Neurosci.* **37**, 161–181 (2014).
6. Z. Chen, Q. Zhou, X. L. Deán-Ben, I. Gezginer, R. Ni, M. Reiss, S. Shoham, D. Razansky, Multimodal noninvasive functional neurophotonic imaging of murine brain-wide sensory responses. *Adv. Sci.* **9**, 2105588 (2022).
7. N. F. Binder, M. E. Amki, C. Glück, W. Middleham, A. M. Reuss, A. Bertolo, P. Thurner, T. Deffieux, C. Lambride, R. Epp, H.-L. Handelsmann, P. Baumgartner, C. Orset, P. Bethge, Z. Kulcsar, A. Aguzzi, M. Tanter, F. Schmid, D. Vivien, M. T. Wyss, A. Luft, M. Weller, B. Weber, S. Wegener, Leptomeningeal collaterals regulate reperfusion in ischemic stroke and rescue the brain from futile recanalization. *Neuron* **112**, 1456–1472.e6 (2024).
8. C. Staehr, R. Rajanathan, D. D. Postnov, L. Hangaard, E. V. Bouzinova, A. Lykke-Hartmann, F. W. Bach, S. L. Sandow, C. Aalkjaer, V. V. Matchkov, Abnormal neurovascular coupling as a cause of excess cerebral vasodilation in familial migraine. *Cardiovasc. Res.* **116**, 2009–2020 (2020).
9. F. Matthews, B. A. Pearlmutter, T. E. Wards, C. Soraghan, C. Markham, Hemodynamics for brain-computer interfaces. *IEEE Signal Process. Mag.* **25**, 87–94 (2008).
10. L.-D. Liao, V. Tsytsarev, I. Delgado-Martínez, M.-L. Li, R. Erzurumlu, A. Vipin, J. Orellana, Y.-R. Lin, H.-Y. Lai, Y.-Y. Chen, N. V. Thakor, Neurovascular coupling: *In vivo* optical techniques for functional brain imaging. *Biomed. Eng. Online* **12**, 38 (2013).

11. K. Masamoto, A. Vazquez, Optical imaging and modulation of neurovascular responses. *J. Cereb. Blood Flow Metab.* **38**, 2057–2072 (2018).

12. R. Cao, J. Li, B. Ning, N. Sun, T. Wang, Z. Zuo, S. Hu, Functional and oxygen-metabolic photoacoustic microscopy of the awake mouse brain. *Neuroimage* **150**, 77–87 (2017).

13. W. Zong, H. A. Obenhaus, E. R. Skytøen, H. Eneqvist, N. L. de Jong, R. Vale, M. R. Jorge, M.-B. Moser, E. I. Moser, Large-scale two-photon calcium imaging in freely moving mice. *Cell* **185**, 1240–1256.e30 (2022).

14. C. Zhao, S. Chen, L. Zhang, D. Zhang, R. Wu, Y. Hu, F. Zeng, Y. Li, D. Wu, F. Yu, Miniature three-photon microscopy maximized for scattered fluorescence collection. *Nat. Methods* **20**, 617–622 (2023).

15. A. Li, H. Guan, H.-C. Park, Y. Yue, D. Chen, W. Liang, M.-J. Li, H. Lu, X. Li, Twist-free ultralight two-photon fiberscope enabling neuroimaging on freely rotating/walking mice. *Optica* **8**, 870–879 (2021).

16. Y. Zhang, L. Yuan, Q. Zhu, J. Wu, T. Nöbauer, R. Zhang, G. Xiao, M. Wang, H. Xie, Z. Guo, Q. Dai, A. Vaziri, A miniaturized mesoscope for the large-scale single-neuron-resolved imaging of neuronal activity in freely behaving mice. *Nat. Biomed. Eng.* **8**, 754–774 (2024).

17. J. Senarathna, H. Yu, C. Deng, A. L. Zou, J. B. Issa, D. H. Hadjiabadi, S. Gil, Q. Wang, B. M. Tyler, N. V. Thakor, A. P. Pathak, A miniature multi-contrast microscope for functional imaging in freely behaving animals. *Nat. Commun.* **10**, 99 (2019).

18. J. Yao, L. V. Wang, Photoacoustic microscopy. *Laser Photonics Rev.* **7**, 758–778 (2013).

19. L. V. Wang, S. Hu, Photoacoustic tomography: In vivo imaging from organelles to organs. *Science* **335**, 1458–1462 (2012).

20. Z. Xu, N. Sun, R. Cao, Z. Li, Q. Liu, S. Hu, Cortex-wide multiparametric photoacoustic microscopy based on real-time contour scanning. *Neurophotonics* **6**, 035012 (2019).

21. J. Ahn, J. W. Baik, D. Kim, K. Choi, S. Lee, S.-M. Park, J. Y. Kim, S. H. Nam, C. Kim, In vivo photoacoustic monitoring of vasoconstriction induced by acute hyperglycemia. *Photoacoustics* **30**, 100485 (2023).

22. G. J. Tserevelakis, D. Soliman, M. Omar, V. Ntziachristos, Hybrid multiphoton and optoacoustic microscope. *Opt. Lett.* **39**, 1819–1822 (2014).

23. B. Rao, F. Soto, D. Kerschensteiner, L. V. Wang, Integrated photoacoustic, confocal, and two-photon microscope. *J. Biomed. Opt.* **19**, 036002 (2014).

24. Y. Wang, S. Hu, K. Maslov, Y. Zhang, Y. Xia, L. V. Wang, In vivo integrated photoacoustic and confocal microscopy of hemoglobin oxygen saturation and oxygen partial pressure. *Opt. Lett.* **36**, 1029–1031 (2011).

25. Y. Wang, K. Maslov, C. Kim, S. Hu, L. V. Wang, Integrated photoacoustic and fluorescence confocal microscopy. *I.E.E.E. Trans. Biomed. Eng.* **57**, 2576–2578 (2010).

26. W. Zhang, Y. Li, Y. Yu, K. Derouin, Y. Qin, V. P. Nguyen, X. Xia, X. Wang, Y. M. Paulus, Simultaneous photoacoustic microscopy, spectral-domain optical coherence tomography, and fluorescein microscopy multi-modality retinal imaging. *Photoacoustics* **20**, 100194 (2020).

27. J. Park, B. Park, T. Y. Kim, S. Jung, W. J. Choi, J. Ahn, D. H. Yoon, J. Kim, S. Jeon, D. Lee, Quadruple ultrasound, photoacoustic, optical coherence, and fluorescence fusion imaging with a transparent ultrasound transducer. *Proc. Natl. Acad. Sci. U.S.A.* **118**, e1920879118 (2021).

28. Z. Chen, S. Yang, D. Xing, Optically integrated trimodality imaging system: Combined all-optical photoacoustic microscopy, optical coherence tomography, and fluorescence imaging. *Opt. Lett.* **41**, 1636–1639 (2016).

29. J. Zhou, W. Wang, L. Jing, S.-L. Chen, Dual-modal imaging with non-contact photoacoustic microscopy and fluorescence microscopy. *Opt. Lett.* **46**, 997–1000 (2021).

30. S.-L. Chen, Z. Xie, L. J. Guo, X. Wang, A fiber-optic system for dual-modality photoacoustic microscopy and confocal fluorescence microscopy using miniature components. *Photoacoustics* **1**, 30–35 (2013).

31. S. Mezil, A. M. Caravaca-Aguirre, E. Z. Zhang, P. Moreau, I. Wang, P. C. Beard, E. Bossy, Single-shot hybrid photoacoustic-fluorescent microendoscopy through a multimode fiber with wavefront shaping. *Biomed. Opt. Express* **11**, 5717–5727 (2020).

32. H. Li, B. Dong, X. Zhang, X. Shu, X. Chen, R. Hai, D. A. Czaplewski, H. F. Zhang, C. Sun, Disposable ultrasound-sensing chronic cranial window by soft nanoimprinting lithography. *Nat. Commun.* **10**, 4277 (2019).

33. X. Zhong, Y. Liang, X. Wang, H. Lan, X. Bai, J. Lin, B.-O. Guan, Free-moving-state microscopic imaging of cerebral oxygenation and hemodynamics with a photoacoustic fiberscope. *Light Sci. Appl.* **13**, 5 (2024).

34. A. D. Elliott, Confocal microscopy: Principles and modern practices. *Curr. Protoc. Cytom.* **92**, e68 (2020).

35. S. Engelhardt, S. Patkar, O. O. Ogunshola, Cell-specific blood–brain barrier regulation in health and disease: A focus on hypoxia. *Br. J. Pharmacol.* **171**, 1210–1230 (2014).

36. K. Kisler, A. R. Nelson, A. Montagne, B. V. Zlokovic, Cerebral blood flow regulation and neurovascular dysfunction in Alzheimer disease. *Nat. Rev. Neurosci.* **18**, 419–434 (2017).

37. V. Fiskum, A. Sandvig, I. Sandvig, Silencing of activity during hypoxia improves functional outcomes in motor neuron networks in vitro. *Front. Integr. Neurosci.* **15**, 792863 (2021).

38. A. Bali, A. S. Jaggi, Electric foot shock stress: A useful tool in neuropsychiatric studies. *Rev. Neurosci.* **26**, 655–677 (2015).

39. S. Sakadžić, E. T. Mandeville, L. Gagnon, J. J. Musacchia, M. A. Yaseen, M. A. Yucel, J. Lefebvre, F. Lesage, A. M. Dale, K. Eikermann-Haerter, C. Ayata, V. J. Srinivasan, E. H. Lo, A. Devor, D. A. Boas, Large arteriolar component of oxygen delivery implies a safe margin of oxygen supply to cerebral tissue. *Nat. Commun.* **5**, 5734 (2014).

40. F. Fernández-Klett, N. Offenhauser, U. Dirnagl, J. Priller, U. Lindauer, Pericytes in capillaries are contractile in vivo, but arterioles mediate functional hyperemia in the mouse brain. *Proc. Natl. Acad. Sci. U.S.A.* **107**, 22290–22295 (2010).

41. P. J. Drew, A. Y. Shih, D. Kleinfeld, Fluctuating and sensory-induced vasodynamics in rodent cortex extend arteriole capacity. *Proc. Natl. Acad. Sci. U.S.A.* **108**, 8473–8478 (2011).

42. R. D. Thijs, R. Surges, T. J. O'Brien, J. W. Sander, Epilepsy in adults. *Lancet* **393**, 689–701 (2019).

43. D. Hadjiabadi, M. Lovett-Barron, I. G. Raikov, F. T. Sparks, Z. Liao, S. C. Baraban, J. Leskovec, A. Losonczy, K. Deisseroth, I. Soltesz, Maximally selective single-cell target for circuit control in epilepsy models. *Neuron* **109**, 2556–2572.e6 (2021).

44. M. Wenzel, J. P. Hamm, D. S. Peterka, R. Yuste, Reliable and elastic propagation of cortical seizures in vivo. *Cell Rep.* **19**, 2681–2693 (2017).

45. T. H. Schwartz, Neurovascular coupling and epilepsy: Hemodynamic markers for localizing and predicting seizure onset. *Epilepsy Curr.* **7**, 91–94 (2007).

46. M. Mitra, A. Kumar, S. Khandare, P. Gaddale, Y. Anandan, S. Pedibhotla, K. Roy, H. Chen, R. Pratap, S. R. Kothapalli, Low-cost scalable PCB-based 2-D transducer arrays for volumetric photoacoustic imaging. *IEEE Sens. J.* **24**, 4380–4386 (2024).

47. B. F. Grewe, F. F. Voigt, M. van 't Hoff, F. Helmchen, Fast two-layer two-photon imaging of neuronal cell populations using an electrically tunable lens. *Biomed. Opt. Express* **2**, 2035–2046 (2011).

48. W. Zong, R. Wu, M. Li, Y. Hu, Y. Li, J. Li, H. Rong, H. Wu, Y. Xu, Y. Lu, H. Jia, M. Fan, Z. Zhou, Y. Zhang, A. Wang, L. Chen, H. Cheng, Fast high-resolution miniature two-photon microscopy for brain imaging in freely behaving mice. *Nat. Methods* **14**, 713–719 (2017).

49. R. Cao, J. Zhao, L. Li, L. Du, Y. Zhang, Y. Luo, L. Jiang, S. Davis, Q. Zhou, A. de la Zerda, L. V. Wang, Optical-resolution photoacoustic microscopy with a needle-shaped beam. *Nat. Photonics* **17**, 89–95 (2023).

50. A. She, S. Zhang, S. Shian, D. R. Clarke, F. Capasso, Adaptive metalenses with simultaneous electrical control of focal length, astigmatism, and shift. *Sci. Adv.* **4**, eaap9957 (2018).

51. R. Shintate, T. Ishii, J. Ahn, J. Y. Kim, C. Kim, Y. Saijo, High-speed optical resolution photoacoustic microscopy with MEMS scanner using a novel and simple distortion correction method. *Sci. Rep.* **12**, 9221 (2022).

52. L. Li, X. Liang, W. Qin, H. Guo, W. Qi, T. Jin, J. Tang, J. Xi, Double spiral resonant MEMS scanning for ultra-high-speed miniaturized optical microscopy. *Optica* **10**, 1195–1202 (2023).

53. H. Guan, D. Li, H.-c. Park, A. Li, Y. Yue, Y.-T. A. Gau, M.-J. Li, D. E. Bergles, H. Lu, X. Li, Deep-learning two-photon fiberscopy for video-rate brain imaging in freely-behaving mice. *Nat. Commun.* **13**, 1534 (2022).

54. T. Vu, A. DiSpirito, D. Li, Z. Wang, X. Zhu, M. Chen, L. Jiang, D. Zhang, J. Luo, Y. S. Zhang, Q. Zhou, R. Horstmeyer, J. Yao, Deep image prior for undersampling high-speed photoacoustic microscopy. *Photoacoustics* **22**, 100266 (2021).

55. J. Chen, H. Sasaki, H. Lai, Y. Su, J. Liu, Y. Wu, A. Zhovmer, C. A. Combs, I. Rey-Suarez, H.-Y. Chang, Three-dimensional residual channel attention networks denoise and sharpen fluorescence microscopy image volumes. *Nat. Methods* **18**, 678–687 (2021).

56. X. Li, G. Zhang, J. Wu, Y. Zhang, Z. Zhao, X. Lin, H. Qiao, H. Xie, H. Wang, L. Fang, Q. Dai, Reinforcing neuron extraction and spike inference in calcium imaging using deep self-supervised denoising. *Nat. Methods* **18**, 1395–1400 (2021).

57. H. Zhao, Z. Ke, F. Yang, K. Li, N. Chen, L. Song, C. Zheng, D. Liang, C. Liu, Deep learning enables superior photoacoustic imaging at ultralow laser dosages. *Adv. Sci.* **8**, 2003097 (2021).

58. Y. Zhang, J. Chen, J. Zhang, J. Zhu, C. Liu, H. Sun, L. Wang, Super-low-dose functional and molecular photoacoustic microscopy. *Adv. Sci.* **10**, 2302486 (2023).

59. L. Sirleto, M. A. Ferrara, Fiber amplifiers and fiber lasers based on stimulated Raman scattering: A review. *Micromachines* **11**, 247 (2020).

60. J. Van Erum, D. Van Dam, P. P. De Deyn, PTZ-induced seizures in mice require a revised Racine scale. *Epilepsy Behav.* **95**, 51–55 (2019).

61. E. A. Pnevmatikakis, A. Giovannucci, NoRMCorre: An online algorithm for piecewise rigid motion correction of calcium imaging data. *J. Neurosci. Methods* **291**, 83–94 (2017).

62. P. Zhou, S. L. Resendez, J. Rodriguez-Romaguera, J. C. Jimenez, S. Q. Neufeld, A. Giovannucci, J. Friedrich, E. A. Pnevmatikakis, G. D. Stuber, R. Hen, M. A. Kheirbek, B. L. Sabatini, R. E. Kass, L. Paninski, Efficient and accurate extraction of in vivo calcium signals from microendoscopic video data. *eLife* **7**, e28728 (2018).

63. A. Brdjanin, N. Dardagan, D. Dzigal, A. Akagic, in *2020 International Conference on INnovations in Intelligent SysTems and Applications (INISTA)* (IEEE, 2020), pp. 1–6.

64. J. Yao, L. Wang, J.-M. Yang, K. I. Maslov, T. T. W. Wong, L. Li, C.-H. Huang, J. Zou, L. V. Wang, High-speed label-free functional photoacoustic microscopy of mouse brain in action. *Nat. Methods* **12**, 407–410 (2015).

65. G. Wissmeyer, M. A. Pleitez, A. Rosenthal, V. Ntziachristos, Looking at sound: Optoacoustics with all-optical ultrasound detection. *Light Sci. Appl.* **7**, 53 (2018).